Design of Interfacial Energy Transfer Model in Upconversion Nanoparticles

Bo Zhou and Jinshu Huang

Abstract The emergence of lanthanide-based upconversion materials provides a feasible solution to the scientific challenges in various fields due to their excellent photon upconversion characteristic and stable physicochemical property. This field benefits greatly from the mechanistic investigation of photon upconversion. In particular, the rational design of interfacial energy transfer (IET) provides a versatile and powerful method to enable and tune the upconversion through precise control of ionic interactions in nanostructures, and further contributes to diversities of frontier applications of upconversion materials. In this chapter, we present a summary and discussion on the design of IET model for upconversion, and demonstrate its unique roles in manipulating energy flux in core–shell nanostructures and mechanistic understanding of ionic interactions on the nanoscale. Its potential in diversities of emerging applications such as information security, upconversion lasers, optical sensing, biological therapy, and lifetime imaging are highlighted. This review would excite new chances for the development of new classes of luminescent materials and further expand their frontier application boundaries.

1 Introduction

Lanthanide-based upconversion nanoparticles (UCNPs) are a typical class of luminescent materials with anti-Stokes emissions [1–3], which have been attracting tremendous attentions for their broad applications in bioimaging [4], therapy [5], display [6], laser [7], sensor [8], and information security [9]. The rich discrete energy levels of lanthanide ions make them an ideal candidate for upconversion emissions covering a wide spectral region from ultraviolet, visible to near infrared wavelength bands. So far, many approaches have been explored to synthesize high-quality core–shell nanocrystals, tune and enhance the upconversion luminescence

B. Zhou (✉) · J. Huang
State Key Laboratory of Luminescent Materials and Devices, School of Materials Science and Engineering, South China University of Technology, Guangzhou 510641, China
e-mail: zhoubo@scut.edu.cn

V. Kumar et al. (eds.), *Upconversion Nanoparticles (UCNPs) for Functional Applications*, Progress in Optical Science and Photonics 24,
https://doi.org/10.1007/978-981-99-3913-8_4

through core–shell engineering, wide-band sensitization, tailoring electromagnetic field, and so on [3, 10–17]. In particular, mechanism investigation plays a critical role in the field of upconversion. Early works showed that energy transfer upconversion is an efficient process for lanthanides (e.g., Er^{3+}, Tm^{3+}, and Ho^{3+}) in both bulk and nanomaterials [1, 18]. Other ways such as excited-state absorption and photon avalanche are also explored to activate upconversion. During past decades, the rapid progress of nanotechnology opens up new possibilities for upconversion [2, 19]. For instance, the $NaGdF_4$@$NaGdF_4$ core–shell nanostructure is able to realize upconversion emissions of lanthanide ions without physically existed intermediate states (e.g., Eu^{3+}, Tb^{3+}, Dy^{3+}, and Sm^{3+}) through the assistance of energy migration over Gd sublattice [20]. However, it should be noted that such upconversion requires specific matrix lattice (e.g., $NaGdF_4$) to facilitate the excitation energy from core to shell layer.

Alternatively, we recently found that interfacial energy transfer (IET) works well in manipulating lanthanide ionic interactions on the nanometer length scale and therefore contributes to photon luminescence from a set of lanthanide ions (e.g., Er^{3+}, Tm^{3+}, Ho^{3+}, Eu^{3+}, Tb^{3+}, Dy^{3+}, Sm^{3+}, Ce^{3+}, Pr^{3+}, and Nd^{3+}) [17, 21]. The design of IET model could enhance upconversion by depressing detrimental ionic interactions such as cross relaxation and back energy transfer [21]. More importantly, it helps to finely tune the emission colors by constructing suitable IET channels in UCNPs [22, 23]. Another important merit lies in the mechanistic research of photon upconversion. Rational design of IET-mediated nanostructures is able to probe the donor–acceptor energy transfer or energy migration at sublattice [2], which is a daunting challenge in the traditional lanthanide-doped bulk or nanosized materials. Recently, the NIR-II responsive upconversion was achieved in a series of lanthanide emitters by taking the advantage of IET processes in multilayer core–shell nanostructures, showing great potential in biophotonics and anti-counterfeiting [9]. Therefore, the design of IET model holds great promise in tuning and optimizing optical performance of upconversion of lanthanide emitters and thus benefitting their emerging frontier applications.

In this chapter, we present a review of the recent progress of IET-mediated upconversion with an emphasis on the design and energy transfer over core–shell interfacial area. We systematically discuss the strategies of manipulating energy transfer pathways to precisely tune upconversion intensity, colors, and lifetime. A deep mechanistic understanding of upconversion including energy transfer and energy migration behaviors on nanometer scale was demonstrated by rational design of IET-mediated structures. We also highlight its frontier applications in multilevel information security, upconversion lasers, optical sensing, biological imaging and therapy. Future challenges are commented in the final section. This review aims to provide a clear demonstration of IET model for upconversion and its possible frontier applications.

2 Energy Flux in Core–shell Nanoparticles

In general, there are three key steps for the energy flux in a upconversion system: injection of infrared excitation energy, energy transfer, and photon irradiation [24, 25]. To minimize the unwanted energy consumption due to the localized energy exchange and other detrimental processes, it is significant to figure out the energy flux in UCNPs before constructing an optimal upconversion system [15, 26, 27]. In this section, we discuss the principles of constructing interfacial region in nanomaterials, which provides an ideal platform for IET model. Typical IET-mediated upconversion processes are presented. The recent strategies for optimization of energy transfer pathway are also illustrated with the aim of amplifying upconversion light intensity and achieving finely tunable colors.

2.1 Construct Interface in Nanomaterials

High-quality interface is a key factor for the construction of IET model. Interestingly, interface widely exists in core–shell structured nanomaterials, and it can be readily achievable by epitaxial growth of shells outside the seed via heat up strategy, Ostwald ripening, and successive layer-by-layer synthetic route. Cation exchange or non-epitaxial growth was also demonstrated useful for constructing heterogeneous core–shell interface [14]. Recently, the inorganic–organic interfaces are also available when specific molecules are attached on the surface of UCNPs [13]. The establishment of core–shell nanoparticles with special interfaces offers an excellent platform to integrate multi-functional properties into a single nanoparticle.

The core–shell-based nanocrystals (e.g., $NaGdF_4$@$NaGdF_4$ and $NaGdF_4$@$NaYF_4$) are a good platform for the IET model [2, 14, 28]. The flexible designs in composition and dopant of each layer provide a facile way to manipulate the physical and optical performance (Fig. 1a). The core–shell nanostructure is easily obtained by wet chemical methods such as coprecipitation and thermal decomposition in an oleic-octadecenoic acid solution, which is evident by the high-resolution TEM image and the distribution of each lanthanide element [29]. It should be pointed out that the lattice mismatch should be small enough to reduce the lattice defect in a given core–shell nanostructure [30]. It is widely demonstrated that sodium rare-earth fluoride shells could be epitaxially grown outside the $NaYF_4$ core by an accurate control of anisotropic strain engineering through tuning of growth affinity [31]. Recently, ultrasmall heterogeneous oxysulfide/fluoride core–shell nanocrystals were synthesized through epitaxial heterogeneous growth [32]. By rationally designing UCNPs with suitable lanthanide dopants and their spatial distribution, interaction across the core–shell interface can be precisely manipulated to engineer optical properties like as the tunable emission colors, lifetimes, and enhanced light intensity [2].

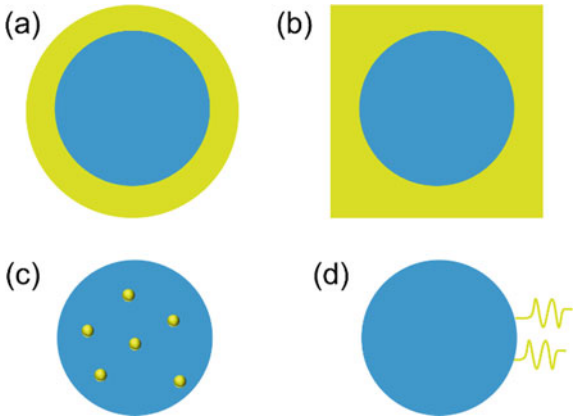

Fig. 1 Construction of different types of interface in nanomaterials. **a** Core with a homogeneous shell. **b** Core with a heterogeneous shell. **c** UCNPs with embedded quantum dots. **d** UCNPs with surface decorated molecules

Besides, there are flourishing other pathways to create interfaces in core–shell nanostructure. More recent research suggested that selective cation exchange could enable growth of β-$NaGdF_4$@CaF_2 core–shell nanoparticles with dissimilar structure [33]. The hetero-structured CaF_2 shell resulted in remarkable upconversion enhancement together with increased quantum yield from 0.2% to 3.7% (Fig. 1b). Upconversion-perovskite core–shell nanoparticles were also reported with tunable emission colors/excitation wavelength and improved stability [34, 35]. $CsPbBr_3$ perovskite and $NaYF_4$:Yb/Tm nanoparticles with different crystal phases and structures were synthesized in the same solution simultaneously with the resultant heterostructure ($CsPbBr_3$ embedded in $NaYF_4$:Yb/Tm), and the violet-blue upconverted emission of Tm^{3+} could be used to activate perovskite upon near infrared excitation (Fig. 1c). A hybrid approach of combining UCNPs and quantum dots/perovskite/dyes is also proved successful to construct special configuration. MoS_2-UCNPs nanocomposite can be synthesized through a controllable two-step thermolysis, which can act as both near infrared sensitizer and excitons generation/separation centers [36]. A mixture of different types of nanoparticles tends to be another convenient and versatile strategy to construct interface with resultant interparticle energy transfer or reabsorption process across two sets of nanoparticles [20, 37, 38]. Dye-sensitized UCNPs are emerging to address the weak upconversion intensity by enlarging absorption of lanthanide ions, and their upconversion quantum yields are heavily dependent on the IET in the hybrid system (Fig. 1d) [13].

2.2 IET-Mediated Upconversion

In principle, efficient energy transfer upconversion occurs in the sensitizer-activator (S-A) coupled system. According to Dexter's theory, the S-A distance is one of the key parameters governing the energy transfer rate which is inversely to the sixth power of S-A separation [1, 18]. It should be noted that IET between specific lanthanide ions

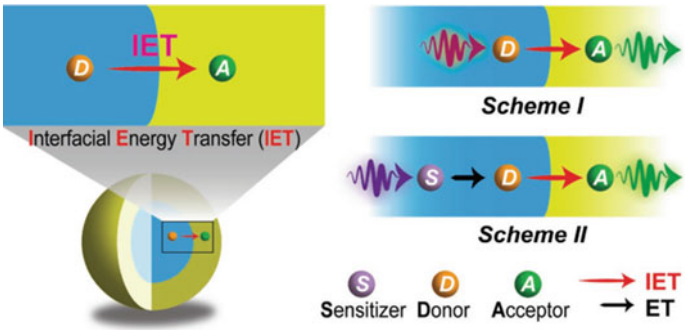

Fig. 2 Mechanistic illustration of IET-mediated upconversion model in core–shell nanostructure with two schemes (I and II). ref. 39, copyright 2018, Wiley–VCH

could also take place when accommodated in different location with a proper spatial separation. As illustrated in Fig. 2, suitable lanthanide ions are selected as energy donor and luminescent acceptor in a core–shell nanostructure respectively. The donor in the core can be activated directly by the external excitation (or via a sensitizer) followed by an IET-mediated energy management toward upconverted emission of the shell (Scheme I). When the donor is non-responsive to the excitation, an additional sensitizer can be added in the core to activate the donor in advance (Scheme II) [39]. It should be noted that an exchange of donors and acceptors locations in such a core–shell structure also enables IET-mediated upconversion.

The IET-mediated upconversion model is able to realize the photon upconversion of a collection of lanthanide ions by selecting a suitable energy donor and acceptor in rationally engineered core–shell nanostructure. For common UCNPs, Yb^{3+} is usually used as a sensitizer owing to its capability in absorbing the 980 nm near infrared photons through $^2F_{5/2} \leftarrow {}^2F_{7/2}$ transition together with subsequent energy transfers to Er^{3+}, Tm^{3+} or Ho^{3+} emitters. To check the possibility of Yb^{3+}-mediated IET upconversion, we constructed the $NaYF_4$:Yb@$NaYF_4$:A(A = Er^{3+}, Tm^{3+}, Ho^{3+}) core–shell nanostructure with a spatial separation of Yb^{3+} and emitters into different layers (Fig. 3a). Typical upconversion emissions of Er^{3+}, Tm^{3+}, and Ho^{3+} were clearly observed with 980 nm irradiation. As a control, almost no upconversion was recorded for the sample without doping Yb^{3+} in the core, further demonstrating the possibility of Yb^{3+}-mediated IET[39]. The use of 808 nm excitation can depress the overheating effect by minimizing the absorption of water molecule, showing great advantages in biological applications. In fact, in an 808 nm-responsive system, Yb^{3+} is also codoped to facilitate the energy transfers from Nd^{3+} to the emitters. Recently, our result showed that Nd^{3+}-to-Yb^{3+} IET process occurring at the core–shell interface also plays a key role in facilitating upconversion (Fig. 3b) [40]. Such an IET process can also be used to tune energy migration over ytterbium lattice, resulting in tunable rise and decay times in a large range [41, 42]. More importantly, a good spectral overlap between Er^{3+} emission ($^4I_{11/2} \rightarrow {}^4I_{15/2}$ transition) and Yb^{3+} absorption ($^2F_{5/2} \leftarrow {}^2F_{7/2}$ transition) enables an efficient IET process from Er^{3+} to Yb^{3+} (Fig. 3c),

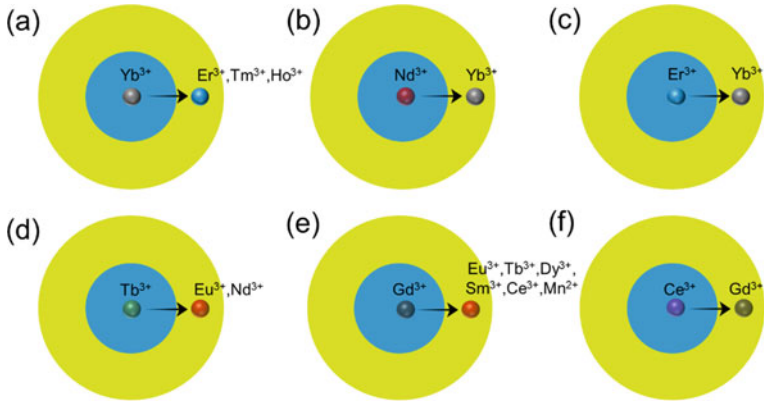

Fig. 3 **a-f** Typical IET processes between energy donor (D) and acceptor (A) in a core–shell nanostructure. **a** D = Yb^{3+}, A = Er^{3+}, Tm^{3+}, Ho^{3+}; **b** D = Nd^{3+}, A = Yb^{3+}; **c** D = Er^{3+}, A = Yb^{3+}; **d** D = Tb^{3+}, A = Eu^{3+}, Nd^{3+}; **e** D = Gd^{3+}, A = Eu^{3+}, Tb^{3+}, Dy^{3+}, Sm^{3+}, Ce^{3+}, Mn^{2+}; **f** D = Ce^{3+}, A = Gd^{3+}

and further contribute to the photon upconversion from a set of lanthanide ions upon 1530 nm excitation [9, 43, 44].

Tb^{3+}-to-Eu^{3+} energy transfer is also a good example which can easily occur in many classes of luminescent materials. Here it is found that Tb^{3+}-mediated IET process is an efficient way to obtain the upconversion of Eu^{3+} by designing $NaYbF_4$:Tb@$NaYF_4$:Eu core–shell nanostructure (Fig. 3d) [45]. At first, the Tb^{3+} can be activated through cooperative sensitization with its upconversion from $^5D_4 \rightarrow {}^7F_J$ (J = 0–6) transitions, and then contribute to the Eu^{3+} emissions at 590 nm ($^5D_0 \rightarrow {}^7F_1$ transition), 615 nm ($^5D_0 \rightarrow {}^7F_2$ transition) and 696 nm ($^5D_0 \rightarrow {}^7F_4$ transition) as a result of Tb^{3+}-to-Eu^{3+} IET process under 980 nm excitation. By monitoring at 544 nm, the markedly reduced lifetime of Tb^{3+} at its $^5D_4$ energy level after doping Eu^{3+} in the shell layer further indicated the dominant energy pathway of IET. Such a Tb^{3+}-mediated IET process was also effective for the activation of Nd^{3+} as evident by the observation of its upconversion emissions at 864 nm ($^4F_{3/2} \rightarrow {}^4I_{9/2}$ transition). On the other hand, the Tb^{3+}-to-Eu^{3+} IET process is helpful to generate a stable yellow-color emission especially at low pump power, which outperforms traditional energy migration-mediated upconversion of Eu^{3+}.

By taking advantage of Gd^{3+}-mediated IET (Fig. 3e), we realized efficient upconversion from a set of lanthanide ions without intermediate energy levels by constructing $NaYbF_4$:Tm/Gd@$NaYF_4$:A (A = Eu^{3+}, Tb^{3+}, Dy^{3+}, Sm^{3+}) core–shell nanostructure [46]. In this design, Gd^{3+} ions are selected as energy donor together with Yb^{3+}/Tm^{3+} as sensitizers under infrared excitation. At 980 nm excitation, typical upconversion emission bands of Eu^{3+}, Tb^{3+}, Dy^{3+}, and Sm^{3+} are clearly recorded. During this process, the lifetime of Gd^{3+} shows a marked decrease. Further investigation suggested that the Gd^{3+}-mediated IET is primarily limited to a 1.5-nm

thick layer away from core–shell interface. Gd^{3+}-mediated IET process is more efficient for photon upconversion in $LiGdF_4$-mediated nanoparticles, showing enhanced Eu^{3+} upconversion in $LiYbF_4$:Y@$LiGdF_4$:Yb/Tm@$LiYF_4$:Eu compared to that of $LiYbF_4$:Y@$LiGdF_4$:Yb/Tm@$LiGdF_4$:Eu. This might be due to the reason that additional energy migration steps lead to more non-radiative energy dissipation [47]. Notably, such a Gd^{3+}-mediated IET process is also applicable to upconversion of Mn^{2+}, which is hardly observable in nanomaterials [48]. The intense ultraviolet-to-visible downshifting emission was also achieved in Gd^{3+}-lattice by Ce^{3+}-to-Gd^{3+} IET process under excitation at 254 nm (Fig. 3f) [23]. More interestingly, the efficient upconversion of Ce^{3+} observed in $NaYbF_4$:Gd/Tm@$NaGdF_4$@CaF_2:Ce core–shell-shell nanostructure further demonstrated the validity of Gd^{3+}-to-Ce^{3+} IET process by tailoring the 4f-5d excitation in CaF_2 host [49]. In contrast to $NaGdF_4$@$NaGdF_4$ core–shell nanostructure, IET-mediated upconversion holds an independent characteristic on the composition of shell matrix, revealing a much more efficient and flexible strategy for controlling of ionic interactions in nanostructure [20, 39].

Despite the above progresses, the narrow and low absorption cross-section (~10^{-20} cm^2) of lanthanide ions limit their capability in injection of energy flux for nanosystem. To overcome this limit, proper molecular dyes (e.g., ICG or IR806) with much larger absorption cross-section of approximately 10^{-17} ~ 10^{-16} cm^2 can be decorated on the surface of UCNPs through ligand exchange strategy to enlarge absorption directly together with a high quantum efficiency of IET from dyes to lanthanide sensitizers [13, 16, 50]. Theoretical analysis indicated that the non-radiative energy transfer from ICG to the surface bound Nd^{3+} ions is pretty efficient with a efficiency reaching to ~57% [51].

More interestingly, recent work showed that upconverted emissions from UCNPs could also give rise to subsequent optical or electronic response of other functional region in a core–shell nanostructure. By taking the advantage of intense ultraviolet upconversion of Tm^{3+}, photon upconversion in perovskite quantum dots with full-color tuning and improved stability was realized through tailoring the perovskite bandgap [35, 37]. The upconverted green luminescence from Yb^{3+}/Er^{3+} couple has a spectral overlap with the absorption band of MoS_2 nanosheets and created excitons generation/separation under 980 nm irradiation, sparking novel interest in near infrared photonic memory with promise in advancing multifunctional robotics [36]. Recent work suggested that the triplet levels of a set of porphyrin and phthalocyanine sensitizers can be effectively activated via direct triplet energy transfer from lanthanide ions to organic molecules with the engagement of IET process to generate cytotoxic singlet oxygen under ultralow near infrared power [52]. It is also possible to control triplet dynamic by coupling organic molecule to UCNPs to turn molecular triplet excitons bright, being essentially important for optoelectronic research [53]. These progresses provide an outstanding approach to the multifunctional lanthanide-doped nanomaterials with versatile properties, further broadening their frontier application in various research fields.

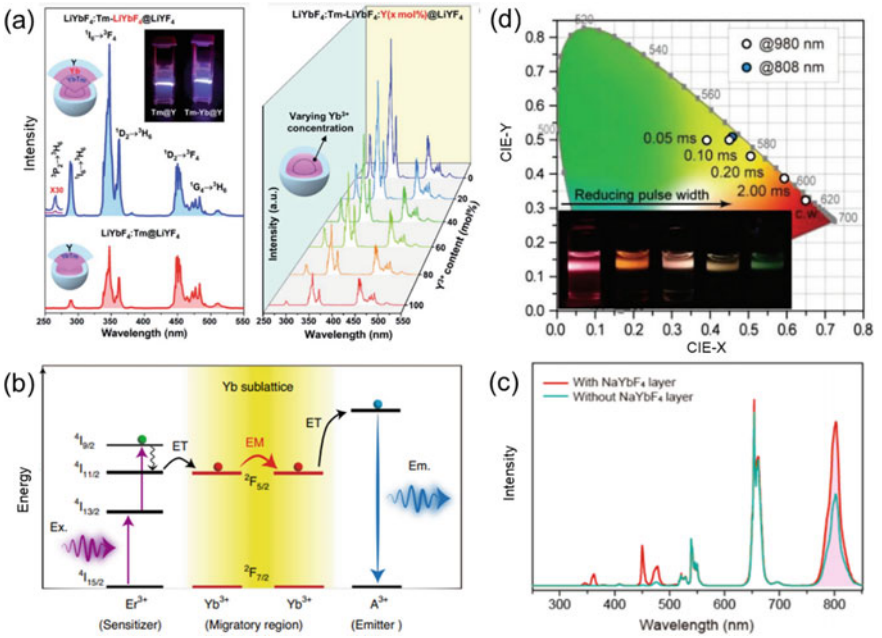

Fig. 4 **a** Left: A comparison of upconversion emission spectra of $LiYbF_4$:Tm@$LiYbF_4$@$LiYF_4$ and $LiYbF_4$:Tm@$LiYF_4$ samples. Right: Upconversion emission spectra of $LiYbF_4$:Tm@$LiYbF_4$:Y(0 ~ 100 mol%)@$LiYF_4$ samples with different Yb^{3+} content in interlayer. **b** Conceptual model for NIR II responsive upconversion. **c** Upconversion emission spectra of $NaErF_4$:Yb/Y@$NaYbF_4$@$NaYF_4$:Yb/Tm@$NaYF_4$ and $NaErF_4$:Yb/Y@$NaYF_4$:Yb/Tm@$NaYF_4$ samples. **d** CIE chromatic coordinates for the upconversion emission profiles from $NaErF_4$:Yb/Tm@$NaYbF_4$ core–shell nanoparticles. **a**, ref. 56, copyright 2021, Royal Society of Chemistry. **b, c**, ref. 9, copyright 2020, Nature Publishing Group. **d**, ref. 22, copyright 2021, Wiley–VCH

2.3 Optimization of Energy Transfer Pathways

According to Laporte selection rule, the *f-f* transitions of lanthanide ions are forbidden, which dramatically impedes their capability for bright upconversion. In order to resolve such intrinsic limit, a collection of strategies was explored to enlarge energy harvest for UCNPs [24, 54, 55]. In the $NaYF_4$:Yb@$NaYF_4$:Er sample with Yb^{3+}-to-Er^{3+} IET process, the emissions of Er^{3+} were obviously improved with a slightly higher quantum yield by comparison to that of $NaYF_4$:Yb/Er owing to the increase of Yb^{3+} concentration (40 mol%) [39]. Intense multiphoton UV upconversion was achieved by adding an additional $LiYbF_4$ interlayer to maximize the 980 nm light absorption in $LiYbF_4$:Tm@$NaYbF_4$@$LiYF_4$. The UV upconversion emissions of Tm^{3+} at 289 and 347 nm indeed increase with elevating Yb^{3+} content in the interlayer (Fig. 4a) [56]. Further, it is possible to switch the excitation wavelength from 980 to 808 nm by using the Nd^{3+}-to-Yb^{3+} IET process, being great importance for the biomedical application. Through decorating suitable amount of ICG molecules, the

upconversion intensity was enhanced by two orders of magnitude via efficient ICG-to-Nd^{3+}-to-Yb^{3+} IET process [40]. Recently, a triplet exciton energy relay-mediated photon upconversion was proposed to enhance the emission intensity of Tb^{3+} by 158 folds, which was attributable to near-unity triplet energy transfer efficiency from lanthanide ions to surface molecules [57].

Another advantage of IET model lies in that spatial separation of donors and acceptors is able to minimize unwanted interfacial interactions to mitigate energy cross-talk, thus contributing to upconversion enhancement. By introducing Yb^{3+} in $NaHoF_4$@$NaYF_4$:Yb@$NaYF_4$ core–shell-shell sample, the Ho^{3+} upconversion was greatly enhanced than that of $NaYbF_4$:Ho@$NaYF_4$ core–shell nanoparticles. As an added benefit, the emission color changed from red to yellow during this process. It should be noted that the strong back energy transfer at the core–shell interfacial region may lead to heavy energy loss as evident in the $NaHoF_4$@$NaYbF_4$@$NaYF_4$ control sample [58]. The Yb^{3+}-Er^{3+} cross-relaxation and Er^{3+}-Yb^{3+} back energy transfer can be substantially suppressed in $NaYF_4$:Er@$NaYbF_4$@$NaYF_4$ structure but still with efficient Yb^{3+}-to-Er^{3+} IET process nearby the core–shell interfacial area. The multiphoton blue upconversion of Er^{3+} was enhanced by 100 folds compared to the traditional core–shell nanoparticles, resulting in a quantum yield up to 6.34% (under excitation power density of 4.5 W cm^{-2}) [59].

Energy migration is another interesting process occurring in identical lanthanide ions with inherent spectral overlap for the absorption/emission transitions, which can assist excitation energy transport over a long distance in sublattice [23]. The IET-mediated process holds a great promise in realizing fine manipulation of energy migration in multilayer core–shell nanostructure toward enhanced upconversion. However, some quenchable interactions may also occur between the neighboring core–shell interfacial area and have to be minimized. We recently found that the upconversion was enhanced by inserting an energy-migratory $NaGdF_4$ interlayer in EMU model via the design of $NaYbF_4$:Tm/Gd@$NaGdF_4$@$NaGdF_4$:A(A = Eu^{3+}, Tb^{3+}, Dy^{3+}, Sm^{3+}) core–shell-shell nanostructure. This design can effectively remove the quenching processes between Tm^{3+} in the core and emitters in the shell [60]. Similar results were observed for the upconversion of Ce^{3+} and Mn^{2+} ions [48, 49]. In addition, the lifetime of lanthanide emitters can be tuned over a large range by the efficient Nd^{3+}-to-Yb^{3+} IET process together with energy migration over Yb sublattice [41, 61].

To date, the excitation wavelengths for most of the present upconversion systems are usually 980 and 808 nm. In order to further shift it to longer infrared spectral region, Er^{3+} was recently checked as a sensitizer to utilize the 1530 nm excitation [62, 63]. However, there exist deleterious quenchable interactions between Er^{3+} and other possible emitters (e.g., Ho^{3+}, Tm^{3+}, Eu^{3+}, and Tb^{3+}) when they are randomly codoped into Er matrix [43, 64]. Rational design of IET channels in a nanostructure may dramatically mitigate uncontrollable energy interactions in Er^{3+}-sensitized upconversion system. Recently, we demonstrated a general strategy for the NIR-II responsive upconversion by constructing an energy-migration mediated core–shell nanostructure. For instance, the Yb sublattice can isolate the deleterious

ionic quenching processes between sensitizers and emitters but still allow for efficient energy transport channel. As shown in $NaErF_4$:Yb/Y@$NaYbF_4$@$NaYF_4$:Yb/Tm@$NaYF_4$ nanostructure (Fig. 4b,c), it could enable efficient Tm^{3+} emission in particular at short-wavelength range under much lower power density (~W cm^{-2}) [9]. More importantly, this design provides a conceptual model to realize the upconversion from a series of lanthanide emitters including Ho^{3+}, Gd^{3+}, Tb^{3+}, and Eu^{3+}. The $NaErF_4$:Ce@$NaYF_4$:Yb/Tm@$NaYF_4$ core–shell-shell nanostructure also helps to observe the upconversion of Tm^{3+} at 1550 nm excitation but needs ultrahigh pumping power density (~kW cm^{-2}) [44]. More recently, we found that the temporal control of interactions between Yb^{3+} and Er^{3+} in a simple $NaErF_4$:Yb/Tm@$NaYbF_4$ core–shell nanostructure provides an approach to the color switchable emission under both steady state and non-steady state excitation [22]. Emission color change was simply obtained by switching excitation wavelength or tuning pulse width of 980 nm laser (Fig. 4d).

3 Mechanistic Understanding of Upconversion by IET

Mechanistic understanding of upconversion processes with complicated energy interactions such as energy transfer, energy migration, and cross-relaxations on the nanoscale is important. However, it remains a challenge for bulk materials or traditional nanoparticles because it is technically impossible to distinguish a given process precisely [21]. Fortunately, the IET-mediated model is ready to figure out specific energy interactions by spatially separating different lanthanide ions in suitable locations in a multilayer core–shell nanostructure, therefore holding great promise in mechanistic understanding and smart control of photon upconversion properties [2, 17].

3.1 Control of Energy Transfer on the Nanoscale

For a dipole energy transfer, its rate is proportional to the inverse of the sixth power of donor–acceptor separation according to Dexter theory [18]. To investigate the energy transfer on the nanometer length scale, we proposed an IET-mediated core–shell-shell nanoarchitecture to spatially separate the donor and acceptor by inserting an inert $NaYF_4$ interlayer (Fig. 5a). Taking the $NaYF_4$:Yb@$NaYF_4$@$NaYF_4$:A (A = Er^{3+}, Tm^{3+}, Ho^{3+}) core–shell-shell nanostructure as an example, the upconverted emission from the outmost layer declines dramatically with increasing $NaYF_4$ interlayer thickness from 0 to 4.5 nm. The emission light intensity decreases to more than one order of magnitude when the interlay thickness reaches about 1.6 nm, thus suggesting that the effective energy transfer is limited to a narrow spatial range around 1.6 nm for Yb^{3+}-A(A = Er^{3+}, Tm^{3+}, Ho^{3+}) system [39]. Increasing the separation can greatly reduce the energy transfer rate which may be compensated by a

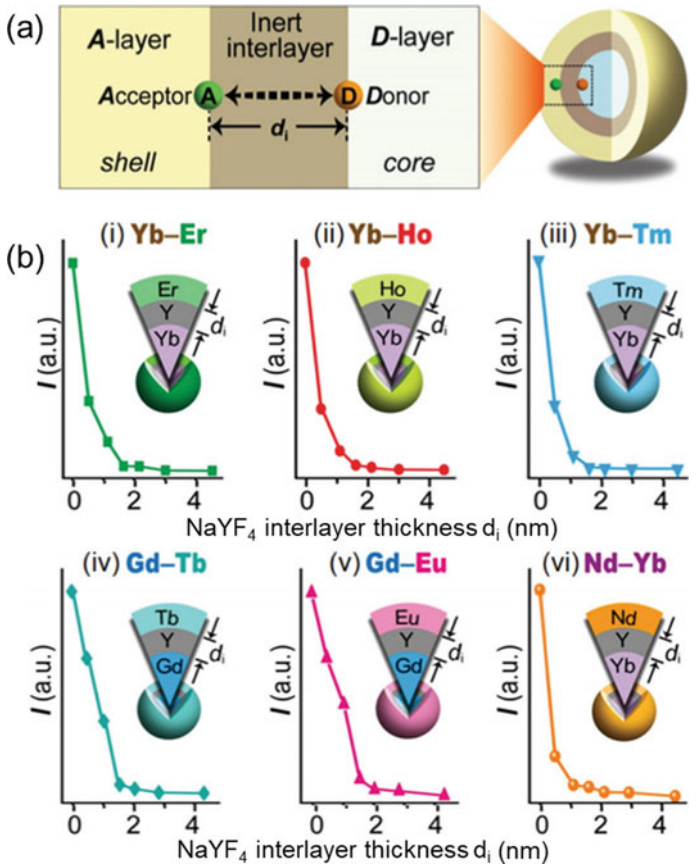

Fig. 5 **a** Proposed core–shell-shell nanostructure to probe donor–acceptor energy transfer by precisely controlling the D-A separation via tuning the thickness of inert interlayer. **b** Upconversion emission intensity as a function of interlayer thickness for (i-iii) $NaYF_4$:Yb@$NaYF_4$@$NaYF_4$:A (A = Er, Ho, Tm) and (iv, v) $NaYbF_4$:Tm/Gd@$NaYF_4$@$NaYF_4$:A (A = Eu, Tb) core–shell-shell nanoparticles under 980 nm excitation, and (vi) $NaYF_4$:Yb/Er@$NaYF_4$@$NaYF_4$:Nd core–shell-shell nanoparticles under 808 nm excitation. ref. 39, copyright 2018, Wiley–VCH

much high power density irradiation [44]. As shown in Fig. 5b, similar result can be observed by constructing $NaYbF_4$:Tm/Gd@$NaYF_4$@$NaYF_4$:A (A = Eu^{3+}, Tb^{3+}) and $NaYF_4$:Yb/Er@$NaYF_4$@$NaYF_4$:Nd core–shell-shell nanostructures, revealing that the effective energy transfer is limited in a range of less than 2.0 nm for Gd^{3+}-Eu^{3+} (or Tb^{3+}) and Nd^{3+}-Yb^{3+} systems. Note that the Gd^{3+}-IET mediated energy transfer distance is appreciably large than Gd^{3+}-Tb^{3+} critical ionic distance (~1.1 nm) [65]. As an added benefit, the emission color of Gd^{3+}-mediated system can be tuned by a precise tuning of $NaYF_4$ interlayer thickness together with a combination of dopant concentration or pump power density. The above results demonstrated the realization of probing lanthanide interactions involved in a set of donor–acceptor pairs,

providing an in-depth insight into the fundamental understanding of energy transfer on the nanoscale, which may help to manipulate and control upconversion at a single nanoparticle level.

3.2 *Probe Energy Migration at Sublattice*

Energy migration process occurring in the identical migratory lanthanide ions plays an important role in precisely engineering the materials structure and moreover manipulating optical properties on the nanometer scale [42]. For example, the excitation energy migration over ytterbium sublattice significantly affects the upconversion dynamics with a resultant tunable rise times in addition to a variable decaying profiles [41, 42, 66]. However, energy migration among sensitizers is technically indistinguishable from energy transfer and other ionic interactions in bulk glasses or conventional nanomaterials. In this regard, our IET-mediated model is able to address the unsatisfactory situation by constructing reasonable core–shell-shell nanostructures and probing energy migration at the sublattice (Fig. 6a) [23].

To investigate the energy migration over Tb sublattice, the $NaYbF_4$:Gd/Tm@$NaYF_4$:Tb@$NaYF_4$:Eu core–shell-shell nanostructures were proposed and confirmed by high-resolution transmission electron microscopy images and elemental mapping profiles (Fig. 6b, c). In this model, the $NaYbF_4$:Gd/Tm, $NaYF_4$:Tb, and $NaYF_4$:Eu functions well as sensitizing core, energy-migration interlayer, and luminescent detecting layer, respectively. It should be noted that Tb^{3+} ions were activated by Gd^{3+}-Tb^{3+} IET process across the interlayer under 980 nm excitation. The upconverted emissions of Eu^{3+} in the detecting layer can be recorded due to the energy migration among Tb sublattice and afterward effective Tb^{3+}-to-Eu^{3+} IET. Thus, the fundamental characteristics of energy migration occurring in the interlayer can be probed by monitoring the typical upconversion emission bands of Eu^{3+}. As shown in Fig. 6d, almost no emission from Eu^{3+} was detected without doping Tb^{3+} in the interlayer, suggesting that the only energy transport channel to activate Eu^{3+} in the outmost shell layer is the IET from Tb^{3+} in interlayer, which can essentially exclude any interference from excitation laser or sensitizing core. The luminescent intensity of Eu^{3+} is closely dependent on the content of Tb^{3+} in the interlayer, and the optimized Tb^{3+} concentration is 70 mol% as evident in the upconversion emission of Eu^{3+}. Therefore, we demonstrate that the energy migration is highly sensitive to the Tb–Tb separation and it becomes a dominant process for high Tb^{3+} doping concentration.

Similarly, the energy migration over Gd and Yb sublattices can also be probed by constructing the $NaYF_4$:Ce@$NaYF_4$:Gd@$NaYF_4$:Eu and $NaYF_4$:Nd@$NaYF_4$:Yb@$NaYF_4$:Er core–shell-shell nanostructures, respectively (Fig. 6e-h). A systematic investigation demonstrated that the non-radiative energy migration behavior is much more efficient than the intrinsic spontaneous emission in Gd^{3+} sublattice, showing better energy migration property than Tb^{3+} and Yb^{3+}, which is in agreement with the reported energy migratory-mediated upconversion

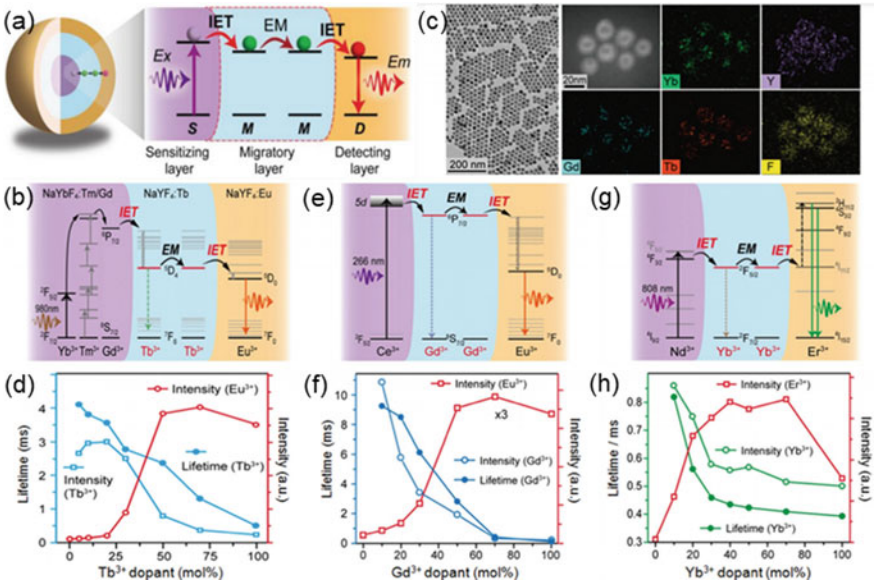

Fig. 6 **a** Proposed IET-mediated core–shell-shell nanostructure to probe energy migration. **b** Schematic of $NaYbF_4$:Gd/Tm@$NaYF_4$:Tb@$NaYF_4$:Eu core–shell-shell nanostructure for probing energy migration over Tb sublattice. (c) TEM, STEM, and element mappings for the **b** sample. **d** Emission intensity of Eu^{3+} (615 nm) and Tb^{3+} (545 nm) and lifetime values of Tb^{3+} (545 nm) as a function of Tb^{3+} concentration in the migratory interlayer. **e** Schematic of $NaYF_4$:Ce@$NaYF_4$:Gd@$NaYF_4$:Eu core–shell-shell nanostructure for probing energy migration over Gd sublattice. **f** Emission intensity of Eu^{3+} (615 nm) and Gd^{3+} (311 nm) and lifetime values of Gd^{3+} (311 nm) as a function of Gd^{3+} concentration in the migratory interlayer. **g** Schematic of $NaYF_4$:Nd@$NaYF_4$:Yb@$NaYF_4$:Er core–shell-shell nanostructure for probing energy migration over Yb sublattice. (h) Emission intensity of Er^{3+} (539 nm) and Yb^{3+} (977 nm) and lifetime values of Yb^{3+} (977 nm) as a function of Yb^{3+} concentration in the migratory interlayer. ref. 23, copyright 2019, Wiley–VCH

in $NaGdF_4$@$NaGdF_4$ system (Fig. 6f). Also, we should note that Yb sublattice exhibits a good energy migration property which is helpful in tuning upconversion dynamics in the Yb-contained systems (Fig. 6h). These results definitely confirmed that the IET-mediated nanostructure is good for probing energy migration behavior on nanometer scale.

3.3 Deep Insight Into Gd^{3+}-Mediated Interfacial Interactions

The IET-mediated upconversion process is widely applicable to realize photon upconversion in a collection of lanthanide ions by a precise control of the existing interactions near the core–shell interfacial area. Moreover, the Gd^{3+}-mediated IET nanostructure has demonstrated its validity for investigation of energy migration over

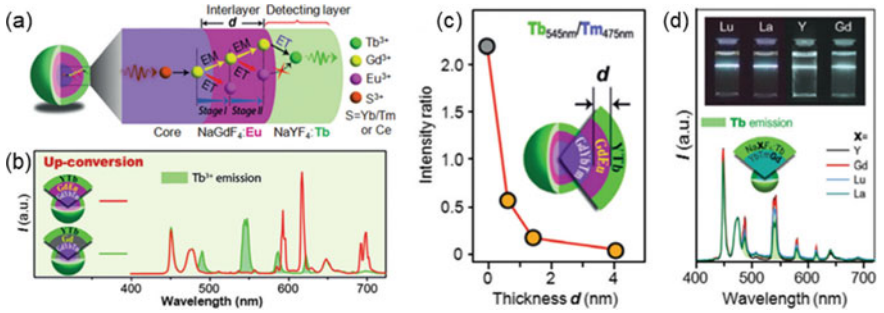

Fig. 7 **a** Schematic of proposed $NaGdF_4$:Yb/Tm@$NaGdF_4$:Eu@$NaYF_4$:Tb core–shell-shell nanostructure for investigation of Gd^{3+}-Gd^{3+} energy migration and Gd^{3+}-to-Eu^{3+} IET by detecting the Tb^{3+} emission from the outermost shell layer. **b** A comparison of upconversion emission spectra of $NaGdF_4$:Yb/Tm@$NaGdF_4$:Eu@$NaYF_4$:Tb and $NaGdF_4$:Yb/Tm@$NaGdF_4$@$NaYF_4$:Tb nanoparticles. **c** Luminescence intensity of Tb^{3+} emission at 545 nm as a function of $NaGdF_4$:Eu interlayer thickness (*d*) for **a** samples under 980 nm excitation. **d** Upconversion emission spectra of $NaYbF_4$:Tm/Gd@$NaXF_4$:Tb(X = Lu, La, Y, Gd) core–shell nanoparticles under 980 nm excitation. (a-c), ref. 46, (d), ref. 39, copyright 2016, 2018, Wiley–VCH

sublattice. In contrast, energy migration-mediated upconversion in conventional $NaGdF_4$@$NaGdF_4$ system only functions well to lanthanide ions without the physically existing intermediate states (e.g., Eu^{3+}, Tb^{3+}, Dy^{3+}, and Sm^{3+}). Note that there may exist a good interface in the $NaGdF_4$@$NaGdF_4$ structure and similar emission phenomenon was observed in the $NaGdF_4$@$NaYF_4$ system. Therefore, a comparative investigation of Gd^{3+}-Gd^{3+} EM and Gd^{3+}-A^{3+} IET would be greatly important for a deep insight into Gd^{3+}-mediated interactions.

In order to figure out the energy migration and energy transfer both of which may occur in the $NaGdF_4$@$NaGdF_4$ core–shell nanostructure, we designed a core–shell-shell sample by coating an additional $NaYF_4$:Tb outmost shell on the typical $NaGdF_4$:Yb/Tm@$NaGdF_4$:Eu nanoparticles (Fig. 7a) [46]. The upconversion of Tb^{3+} is heavily dependent on the Gd^{3+}-Gd^{3+} energy migration in the $NaGdF_4$:Eu interlayer due to the energy transfer block from Eu^{3+} to Tb^{3+} at the core/shell interface. Strikingly, the upconversion intensity of Tb^{3+} showed a rapid decline with increasing $NaGdF_4$:Eu thickness and nearly vanished when the interlayer thickness reached 4.0 nm, implying that the energy migration only works within a narrow layer close to the core/interlayer interface (Fig. 7b, c). This suggests an existence of competition between the interfacial energy transfer and energy migration, and moreover the interfacial energy transfer contributes a lot to the photon upconversion of $NaGdF_4$ shell compared to Gd^{3+}-Gd^{3+} energy migration behavior (Fig. 7d) [39]. In order to understand the underlying mechanism that resulted in the difference between the above two energy interactions, the decaying lifetime of Gd^{3+} for its $^6P_{7/2} \rightarrow {}^8S_{7/2}$ transition was measured and monitored at 311 nm under a pulsed 980 nm laser excitation, exhibiting a gradual decline for $NaGdF_4$:Yb/Tm@$NaYF_4$, $NaGdF_4$:Yb/

$Tm@NaGdF_4$, and $NaGdF_4$:Yb/Tm@$NaYF_4$:Eu core–shell samples. This observation further experimentally demonstrated that IET across the interfacial core–shell area is much more efficient than energy migration.

4 Frontier Applications

Over the past few years, the rapid development of IET-mediated upconversion process has enabled nanomaterials with specific optical property and thus boosted broad frontier applications ranging from biological fields to nanophotonics. In this section, we attempt to highlight the broad utility of IET-mediated upconversion process in information security [9, 22, 23], upconversion lasers [44, 49], optical sensing [67], biological therapy [68, 69], and lifetime imaging [70].

4.1 Information Security and Anti-Counterfeiting

The emergence of counterfeit goods in contemporary markets causes huge economic loss and triggers anxiety about copyright and intellectual property. The research on the field of anti-counterfeiting technology has been witnessing a worldwide rapid development in materials science and the availability of decoding method [71, 72]. Specially, the IET-mediated upconversion from lanthanide-based optical nanomaterials has recently led to a large pavement to anti-counterfeiting applications alignment to the well-engineered property. A smart control of IET in $NaErF_4@NaYbF_4$ provided additional opportunity for information security by switching excitation wavelengths to decode specific hidden information (Fig. 8a) [9]. The unique temporal characteristics of Er^{3+}-Yb^{3+} interactions nearby the core–shell interfacial area can enable the color-switchable output by tuning the pulse width of 980 nm irradiation laser (Fig. 8b) [22]. A distinguishable color was also obtainable through using the pulse excitation in $NaYF_4$:Ho@$NaYF_4$:Yb@$NaYF_4$ inks, further providing an additional temporal feature for multi-level anti-counterfeiting [58]. The thermochromic upconversion also creates new candidate for information security and multi-level anticounterfeiting as evident in tetragonal $LiErF_4@LiYF_4$ core–shell nanoparticles [73, 74].

Besides, the lanthanide ions (or Mn^{2+}) with different lifetimes and distinct emission colors could offer an alternative solution to multi-level information security of trademark patterns by taking the advantage of time-gating technology. For example, the pattern of lotus with a red flower and a green leaf was clearly distinguished from a dazzled light by filtering emissions with much short lifetime than Eu^{3+} and Tb^{3+} (Fig. 8c) [23]. A blue, red, and green color with specific pattern information can be observed by tuning the width of time-gating observing window when Mn^{2+} is further introduced (Fig. 8d) [48]. Recently, a nanocomposite of $NaGdF_4$:Yb/Tm@$NaYF_4$:Tb nanoparticles and EuSe semiconductor was synthesized by cation

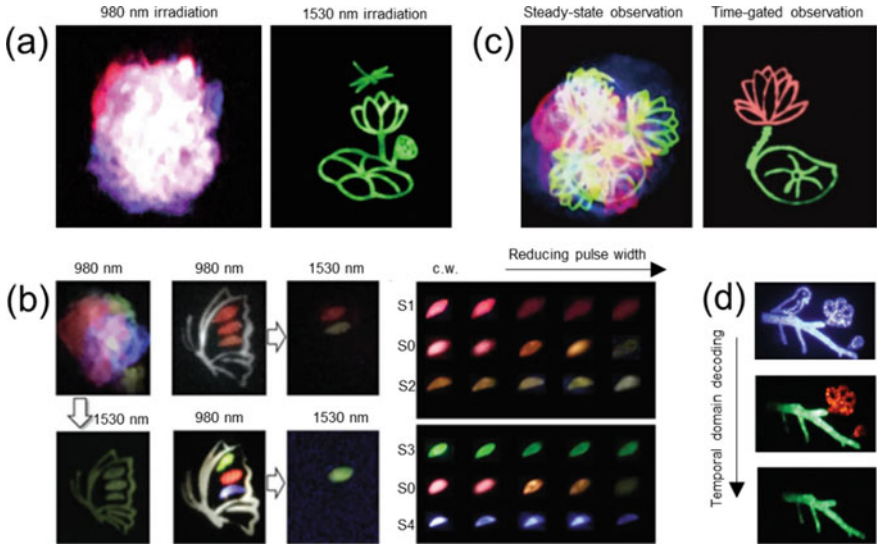

Fig. 8 **a** Decoding the "dragonfly-on-lotus" pattern by switching excitation wavelength from 980 to 1530 nm (right), which presents as dazzle light under conventional 980 nm irradiation (left). **b** Decoding the concealed information through the 1530 nm irradiation from a dazzle light under 980 nm irradiation (left). Detailed information on the wings of the butterfly pattern was revealed by switching excitation wavelength (middle). Color-switchable output under 980 nm non-steady-state excitation (right). **c** The pattern of lotus observed at the steady-state and the time-gating state at 808 nm irradiation. **d** The pattern color recorded under 980 steady-state excitation (top) and that recorded after processing by the time-gating technology (middle and bottom). **a**, ref. 9, copyright 2020, Nature Publishing Group. **b**, ref. 22, (**c**), ref. 23, copyright 2021, 2019, Wiley–VCH. **d**, ref. 48, copyright 2021, the Royal Society of Chemistry

exchange method, which demonstrated advanced optical anti-counterfeiting and information storage through the IET [75].

4.2 Upconversion Laser

Micro-nano lasers have wide applications in nanophotonics and bioelectronics. The ever-increasing demand for miniaturized lasers promotes the pursuit of micro- or nano-sized cavity for on-chip integration [76]. However, the reduction in cavity size generally increases optical losses and requires higher pump powers to reach lasing thresholds [77]. In search of more efficient gain materials in lasing application, lanthanide-based nanomaterials recently have captured increasing interests. Amplified spontaneous emission was first observed from a Fabry–Perot cavity containing $NaYF_4$:Yb/Er@$NaYF_4$ dispersed cyclohexane solution [78]. The realization of ultraviolet upconversion emission of Ce^{3+} via an IET-mediated process

in α-$NaYbF_4$:Gd/Tm@$NaGdF_4$@CaF_2:Ce nanoparticles provided a novel opportunity for the development of ultraviolet laser (Fig. 9a, b) [49]. Very recently, the $NaErF_4$:Ce@$NaYF_4$:Yb/Tm@$NaYF_4$ core–shell-shell nanostructure was developed to achieve a deep-ultraviolet emission at 290 nm under excitation of telecommunication wavelength at 1550 nm with the engagement of efficient Er^{3+}-to-Yb^{3+} IET process [44]. A toroidal microresonator cavity incorporated with as-synthesized nanoparticles supported whispering gallery model, resulting in single-model lasing at 289.2 nm with a high-quality factor of about 2×10^5, which was able to sensitive detection of small biological species (Fig. 9c,d). A structural optimization for IET-mediated model may trigger some new ideas and solutions that expand the scope of designing nano-sized lasers with low action threshold.

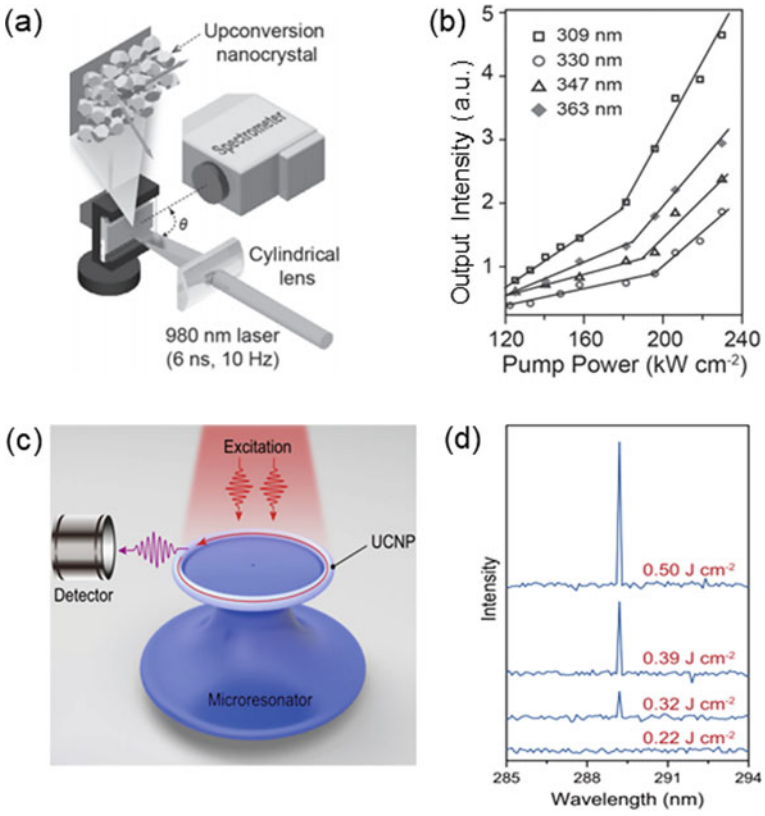

Fig. 9 **a** Schematic of the experimental setup for laser measurement. **b** Output light intensity as a function of excitation power for the α-$NaYbF_4$:Gd/Tm(40/1 mol%)@$NaGdF_4$@CaF_2:Ce(15 mol%) sample. **c** Schematic of the microtoroidal resonator platform for upconversion lasing. **d** Emission spectra of a microresonator with $D_m = 17$ μm at different excitation powers. **a**, **b**, ref. 49, copyright 2017, Wiley–VCH. (**c**, **d**), ref. 44, copyright 2022, Nature Publishing Group

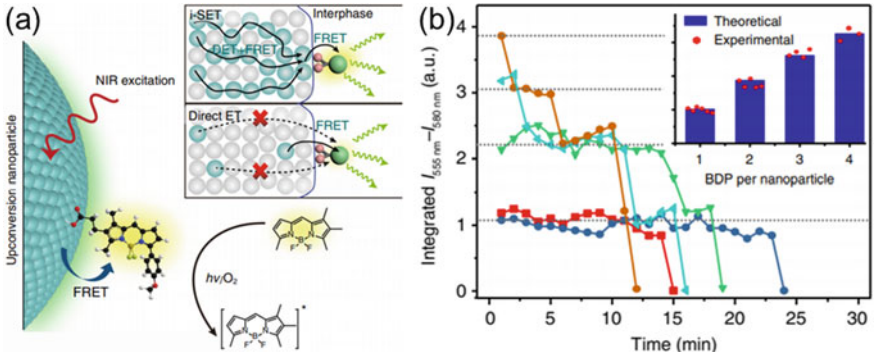

Fig. 10 **a** Schematic of molecular sensing based on a single UCNP. **b** Time-dependent integrated emission intensity changes of BDP recorded from several individual single-particle measurements. ref. 81, copyright 2020, Nature Publishing Group

4.3 Single-Particle Imaging and Sensing

The capability of lanthanide-based upconversion nanomaterials with non-blinking and high photostable properties shows great potential in single-particle imaging and sensing [79, 80]. An interparticle-surface energy transfer model was proposed by adopting the Tb^{3+}-activator-rich core–shell nanostructure to drastically enhance the non-radiative interfacial energy transfer from lanthanide emitters to surface-decorated fluorescent molecules, resulting in a spectroscopically distinguishable emission at a single-particle level (Fig. 10). The rational selection of Tb^{3+} ions can impede energy transfer to surface quenching sites but still allow for efficient energy transfer to surface molecules as a result of their relatively high lowest emitting levels ($^5D_4$) and spectral overlapping between their visible emission and absorption of organic fluorophores [81]. The precise control of energy migration among different energy levels of a single lanthanide emitter produced excitation-emission orthogonal upconversion, which could be utilized to detect explosive residues in the fingerprint and rapid quantitative detections of grain toxin [8, 82].

4.4 Biotherapy

The deep penetration depth of NIR excitation wavelength also has access to a powerful multifunctional platform for biotherapy. The generation of reactive oxygen species (ROS) holds great promise in photodynamic therapy and synthetic chemistry [83, 84]. The intense emission from high-energy levels of lanthanide emitters offers opportunities for deep-tissue biophotonics [59]. However, under ultraviolet irradiation, the spin-forbidden characteristic of electronic transition from single ground state to triplet excited state causes energy loss with resultant inadequate production

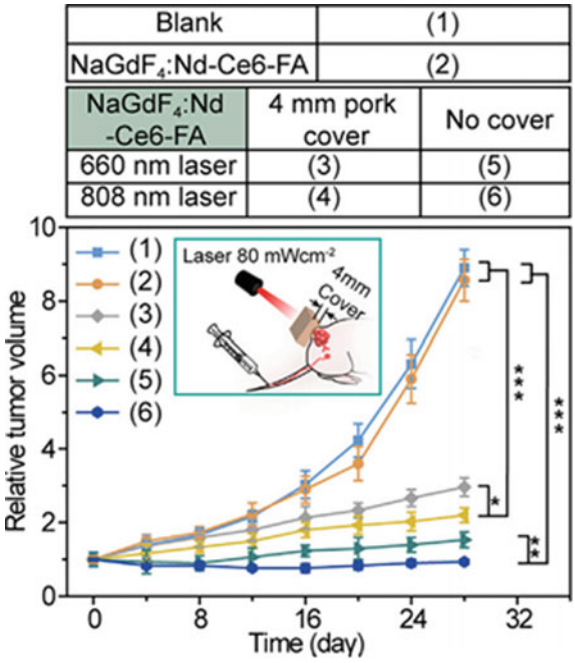

Fig. 11 Changes in relative tumor volume of SKOV3 tumor-bearing mice in response to different treatments. ref. 52, copyright 2021, Elsevier Publishing Group

of ROS. Recent work demonstrated that the lanthanide emitter could sensitize the triplet state of photosensitizers directly to suppress unwanted energy dissipation, providing opportunity for deep-tissue ablation and cancer therapy (Fig. 11) [52, 85].

4.5 Lifetime Imaging

Luminescence lifetime imaging has shown critical advantages over traditional optical imaging owing to their intrinsic stability. The long lifetime of lanthanide-based nanomaterials can be precisely tuned over large tunable range facilitated by IET-mediated upconversion and be easily distinguishable from background during imaging procedure. For instance, high-capacity upconversion wavelength and lifetime binary encoding demonstrated exponentially scalable encoding capacity and opened new opportunity for optical multiplexing with the engagement of Nd^{3+}-to-Yb^{3+} IET process and the following energy migration over Yb sublattice, which provided a controllable lifetime values [86]. This strategy is also applicable to creating a tunable lifetime in downshifting nanoparticles and thus leads to lifetime-engineered NIR-II multiplexed in vivo imaging (Fig. 12) [41].

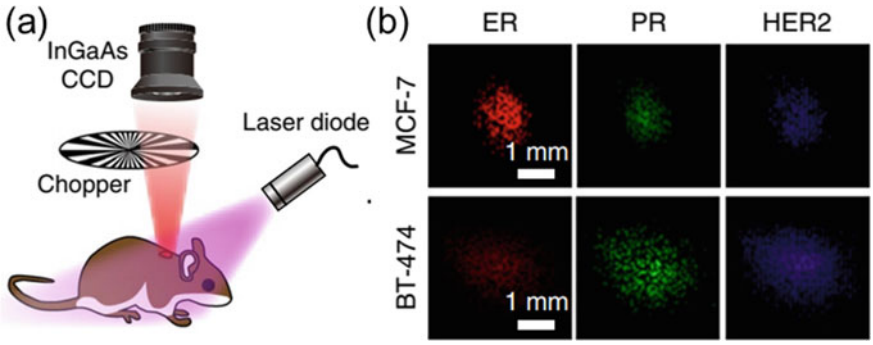

Fig. 12 **a** Home-build lifetime imaging experimental systems. **b** Lifetime-resolved images for the MCF-7 and BT-474 tumors are decomposed into the three lifetime channels, represented by the red, green, and blue monochromatic image sets. ref. 41 copyright 2018, Nature Publishing Group

5 Conclusions

In conclusion, we have briefly summarized the recent progress of IET-mediated upconversion from the aspects of nanostructure design together with the advancing strategy of optical manipulation. The rational construction of IET in a suitable multilayer nanostructure holds great promise in manipulation of energy flux in upconversion system with improved light intensity and quantum efficiency. The IET-mediated upconversion process is also applicable for investigation of energy transfer on the nanometer scale and probing energy migration over sublattice, which provides an in-depth fundamental understanding of photon upconversion. The design of IET has been demonstrated to be a novel and efficient pathway to achieve and manipulate photon upconversion, further opening up a door for the development of information security, upconversion laser, optical sensing, and biological imaging.

Despite remarkable progresses during the past years, there remain challenges regarding research on IET model in the future:

i. *Constructing controllable core–shell interface.* The construction of controllable interface in nanomaterials plays a critical role in the optical modulation and its application [30, 87]. Different designs of interface hold specific functions such as optical, catalytic, and magnetic characteristics. This means that a suitable mismatch in lattice may expand the design of interface, and synthesis of hetero-core–shell nanostructure (e.g., β-$NaGdF_4$@CaF_2) becomes a possible way [88, 89]. The research in this field would further expand the scope of tunable optical properties to amplify the sensibility in temperature and stress [74, 90].
ii. *Further enhancement of upconversion intensity.* One key problem regarding upconversion nanomaterials lies in the weak light intensity compared to the bulk. IET-mediated upconversion process can suppress unwanted energy interactions by spatially separating dopants into different layers. While we have to note that such separation may also lead a decline in energy transfer efficiency. The

research for new strategies to minimize the deleterious interactions and develop facile methods for designs of new IET model helps in addressing such problem.

iii. *Research on the ion diffusion at interface.* High-quality interface closely depends on the shell growth conditions (e.g., temperature, the size of core seeds, and shell thickness) [2, 91, 92]. Ion diffusion may occur in the core–shell interfacial area, which can produce a significant influence on the final luminescence performance. For example, the elemental migration of Er^{3+} in $NaErF_4$@$NaYF_4$ core–shell nanostructure led to a change in emission profiles by tuning the annealing temperature [91]. However, the underlying mechanism of critical ion diffusion remains to be unclear and needs further research.

iv. *Theoretical simulation of ionic interactions at the interfacial area.* Theoretical simulation helps in stimulating new chances for the mechanistic understanding of energy migration, surface quenching, and cross relaxation through using Monto Carlo simulation or other specific models [42, 93]. Density functional theory (DFT) calculation demonstrated that the electron charge density of the crystal surface increased after replacement of Gd^{3+} by Y^{3+} in the crystal lattice, resulting in a size evolution of $NaYF_4$:Yb/Er nanoparticles [19]. Theoretical modeling and simulation may trigger some ideas and solutions to investigation of ionic interactions at the interfacial area.

v. *Design of the organic–inorganic interface.* Recently, the organic–inorganic composite nanomaterials have attracted increasing attentions owing to their advantages for amplifying upconversion and lighting triplet excitons [13, 53, 57]. The suitable organic molecules can be easily anchored on the surface of UCNPs through simple physicochemical strategy. However, there exists complicated energy interactions in such organic–inorganic nanocomposite systems, to which a close attention should be paid in order to figure out the underlying mechanisms.

Overall, this chapter provides an informative review on the IET model in upconversion materials together with its unique roles in mechanistic understanding of photoluminescence processes, both of which contribute to diversities of frontier applications. We believe that a smart design and control of IET model would continuously promote the research of this field with a multidisciplinary collaboration in the near future.

References

1. B. Zhou, B. Shi, D. Jin, X. Liu, Nat. Nanotechnol. **10**, 924–936 (2015)
2. S. Liu, L. Yan, J. Huang, Q. Zhang, B. Zhou, Chem. Soc. Rev. **51**, 1729–1765 (2022)
3. B. Zheng, J. Fan, B. Chen, X. Qin, J. Wang, F. Wang, R. Deng, X. Liu, Chem. Rev. **122**, 5519–5603 (2022)
4. H. Dong, L.-D. Sun, C.-H. Yan, Nano Today **35**, 100956 (2020)
5. Y. Yang, J. Huang, W. Wei, Q. Zeng, X. Li, D. Xing, B. Zhou, T. Zhang, Nat. Commun. **13**, 3149 (2022)
6. R. Deng, F. Qin, R. Chen, W. Huang, M. Hong, X. Liu, Nat. Nanotechnol. **10**, 237–242 (2015)

7. B.-S. Moon, T.K. Lee, W.C. Jeon, S.K. Kwak, Y.-J. Kim, D.-H. Kim, Nat. Commun. **12**, 4437 (2021)
8. Z. Lei, X. Ling, Q. Mei, S. Fu, J. Zhang, Y. Zhang, Adv. Mater. **32**, 1906225 (2020)
9. B. Zhou, L. Yan, J. Huang, X. Liu, L. Tao, Q. Zhang, Nat. Photonics **14**, 760–766 (2020)
10. X. Liu, C.-H. Yan, J.A. Capobianco, Chem. Soc. Rev. **44**, 1299–1301 (2015)
11. W. Feng, X. Zhu, F. Li, NPG Asia Mater. **5**, e75 (2013)
12. W. Zheng, P. Huang, D. Tu, E. Ma, H. Zhu, X. Chen, Chem. Soc. Rev. **44**, 1379–1415 (2015)
13. S. Wen, J. Zhou, P.J. Schuck, Y.D. Suh, T.W. Schmidt, D. Jin, Nat. Photonics **13**, 828–838 (2019)
14. Y. Fan, L. Liu, F. Zhang, Nano Today **25**, 68–84 (2019)
15. L. Tu, X. Liu, F. Wu, H. Zhang, Chem. Soc. Rev. **44**, 1331–1345 (2015)
16. W. Zou, C. Visser, J.A. Maduro, M.S. Pshenichnikov, J.C. Hummelen, Nat. Photonics **6**, 560–564 (2012)
17. J. Huang, L. Yan, S. Liu, L. Tao, B. Zhou, Mater. Horizon. **9**, 1167–1195 (2022)
18. F. Auzel, Chem. Rev. **104**, 139–174 (2004)
19. F. Wang, Y. Han, C.S. Lim, Y. Lu, J. Wang, J. Xu, H. Chen, C. Zhang, M. Hong, X. Liu, Nature **463**, 1061–1065 (2010)
20. F. Wang, R. Deng, J. Wang, Q. Wang, Y. Han, H. Zhu, X. Chen, X. Liu, Nat. Mater. **10**, 968–973 (2011)
21. B. Zhou, Q. Li, L. Yan, Q. Zhang, J. Rare Earths **38**, 474–482 (2020)
22. J. Huang, L. Yan, S. Liu, N. Song, Q. Zhang, B. Zhou, Adv. Funct. Mater. **31**, 2009796 (2021)
23. B. Zhou, J. Huang, L. Yan, X. Liu, N. Song, L. Tao, Q. Zhang, Adv. Mater. **31**, 1806308 (2019)
24. L. Liang, X. Qin, K. Zheng, X. Liu, Acc. Chem. Res. **52**, 228–236 (2019)
25. X. Qin, J. Xu, Y. Wu, X. Liu, A.C.S. Cent, Sci. **5**, 29–42 (2019)
26. B. Chen, F. Wang, Acc. Chem. Res. **53**, 358–367 (2020)
27. H. Zhang, Z.-H. Chen, X. Liu, F. Zhang, Nano Res. **13**, 1795–1809 (2020)
28. F. Wang, R. Deng, X. Liu, Nat. Protoc. **9**, 1634–1644 (2014)
29. M. Wu, L. Yan, T. Wang, B. Zhou, Q. Zhang, Adv. Funct. Mater. **29**, 1804160 (2019)
30. J. Zhao, B. Chen, F. Wang, Adv. Mater. **32**, 2004142 (2020)
31. J. Zhao, X. Chen, B. Chen, X. Luo, T. Sun, W. Zhang, C. Wang, J. Lin, D. Su, X. Qiao, F. Wang, Adv. Funct. Mater. **29**, 1903295 (2019)
32. Q. Zou, C. Marcelot, N. Ratel-Ramond, X. Yi, P. Roblin, F. Frenzel, U. Resch-Genger, A. Eftekhari, A. Bouchet, C. Coudret, M. Verelst, X. Chen, R. Mauricot, C. Roux, ACS Nano (2022). https://doi.org/10.1021/acsnano.2c02423
33. H. Dong, L.-D. Sun, L.-D. Li, R. Si, R. Liu, C.-H. Yan, J. Am. Chem. Soc. **139**, 18492–18495 (2017)
34. H. Xiao, B. Liu, L. Qiu, G. Li, G. Zhang, D. Huang, Y. Zhao, C. Yang, F. Jiang, P. Dang, H. Lian, Z. Cheng and J. Lin, Angew. Chem., Int. Ed., 2022, **61**, e202115136.
35. L. Ruan, Y. Zhang, Nat. Commun. **12**, 219 (2021)
36. Y. Zhai, X. Yang, F. Wang, Z. Li, G. Ding, Z. Qiu, Y. Wang, Y. Zhou, S.-T. Han, Adv. Mater. **30**, 1803563 (2018)
37. W. Zheng, P. Huang, Z. Gong, D. Tu, J. Xu, Q. Zou, R. Li, W. You, J.-C.G. Bünzli, X. Chen, Nat. Commun. **9**, 3462 (2018)
38. M.A. van de Haar, A.C. Berends, M.R. Krames, L. Chepyga, F.T. Rabouw, A. Meijerink, J. Phys. Chem. Lett. **11**, 689–695 (2020)
39. B. Zhou, L. Yan, L. Tao, N. Song, M. Wu, T. Wang, Q. Zhang, Adv. Sci. **5**, 1700667 (2018)
40. N. Song, B. Zhou, L. Yan, Q. Zhang, Front. Chem **6**, 673 (2019)
41. Y. Fan, P. Wang, Y. Lu, R. Wang, L. Zhou, X. Zheng, X. Li, J.A. Piper, F. Zhang, Nat. Nanotechnol. **13**, 941–946 (2018)
42. J. Zuo, D. Sun, L. Tu, Y. Wu, Y. Cao, B. Xue, Y. Zhang, Y. Chang, X. Liu, X. Kong, W. J. Buma, E. J. Meijer, H. Zhang, Angew. Chem., Int. Ed., 2018, **57**, 3054–3058.
43. X. Cheng, Y. Pan, Z. Yuan, X. Wang, W. Su, L. Yin, X. Xie, L. Huang, Adv. Funct. Mater. **28**, 1800208 (2018)

44. T. Sun, B. Chen, Y. Guo, Q. Zhu, J. Zhao, Y. Li, X. Chen, Y. Wu, Y. Gao, L. Jin, S.T. Chu, F. Wang, Nat. Commun. **13**, 1032 (2022)
45. B. Zhou, W. Yang, S. Han, Q. Sun, X. Liu, Adv. Mater. **27**, 6208–6212 (2015)
46. B. Zhou, L. Tao, Y. Chai, S. P. Lau, Q. Zhang and Y. H. Tsang, Angew. Chem., Int. Ed., 2016, **55**, 12356–12360
47. S. Liu, L. Yan, Q. Li, J. Huang, L. Tao, B. Zhou, Chem. Eng. J. **397**, 125451 (2020)
48. L. Yan, X. Wang, Z. An, Z. Hu, H. Liu, S. Xu, B. Zhou, Nanoscale **13**, 13995–14000 (2021)
49. X. Chen, L. Jin, T. Sun, W. Kong, S.F. Yu, F. Wang, Small **13**, 1701479 (2017)
50. G. Chen, J. Damasco, H. Qiu, W. Shao, T.Y. Ohulchanskyy, R.R. Valiev, X. Wu, G. Han, Y. Wang, C. Yang, H. Ågren, P.N. Prasad, Nano Lett. **15**, 7400–7407 (2015)
51. W. Wei, G. Chen, A. Baev, G.S. He, W. Shao, J. Damasco, P.N. Prasad, J. Am. Chem. Soc. **138**, 15130–15133 (2016)
52. B. Zheng, D. Zhong, T. Xie, J. Zhou, W. Li, A. Ilyas, Y. Lu, M. Zhou, R. Deng, Chem **7**, 1615–1625 (2021)
53. S. Han, R. Deng, Q. Gu, L. Ni, U. Huynh, J. Zhang, Z. Yi, B. Zhao, H. Tamura, A. Pershin, H. Xu, Z. Huang, S. Ahmad, M. Abdi-Jalebi, A. Sadhanala, M.L. Tang, A. Bakulin, D. Beljonne, X. Liu, A. Rao, Nature **587**, 594–599 (2020)
54. S. Wen, J. Zhou, K. Zheng, A. Bednarkiewicz, X. Liu, D. Jin, Nat. Commun. **9**, 2415 (2018)
55. H. Dong, L.-D. Sun, C.-H. Yan, Chem. Soc. Rev. **44**, 1608–1634 (2015)
56. S. Liu, J. Huang, L. Yan, N. Song, P. Zhang, J. He, B. Zhou, J. Mater. Chem. A **9**, 4007–4017 (2021)
57. S. Han, Z. Yi, J. Zhang, Q. Gu, L. Liang, X. Qin, J. Xu, Y. Wu, H. Xu, A. Rao, X. Liu, Nat. Commun. **12**, 3704 (2021)
58. R. Huang, S. Liu, J. Huang, H. Liu, Z. Hu, L. Tao, B. Zhou, Nanoscale **13**, 4812–4820 (2021)
59. B. Zhou, B. Tang, C. Zhang, C. Qin, Z. Gu, Y. Ma, T. Zhai, J. Yao, Nat. Commun. **11**, 1174 (2020)
60. X. Wang, L. Yan, S. Liu, P. Zhang, R. Huang, B. Zhou, Nanoscale **12**, 18807–18814 (2020)
61. H. Li, M. Tan, X. Wang, F. Li, Y. Zhang, L. Zhao, C. Yang, G. Chen, J. Am. Chem. Soc. **142**, 2023–2030 (2020)
62. N.J. Johnson, S. He, S. Diao, E.M. Chan, H. Dai, A. Almutairi, J Am Chem Soc **139**, 3275–3282 (2017)
63. Q. Chen, X. Xie, B. Huang, L. Liang, S. Han, Z. Yi, Y. Wang, Y. Li, D. Fan, L. Huang and X. Liu, Angew. Chem., Int. Ed., 2017, **56**, 7605–7609
64. L. Yan, B. Zhou, N. Song, X. Liu, J. Huang, T. Wang, L. Tao, Q. Zhang, Nanoscale **10**, 17949–17957 (2018)
65. Q. Su, S. Han, X. Xie, H. Zhu, H. Chen, C.-K. Chen, R.-S. Liu, X. Chen, F. Wang, X. Liu, J. Am. Chem. Soc. **134**, 20849–20857 (2012)
66. X. Liu, Z.-H. Chen, H. Zhang, Y. Fan and F. Zhang, Angew. Chem., Int. Ed., 2021, **60**, 7041–7045.
67. Z. Zhang, S. Shikha, J. Liu, J. Zhang, Q. Mei, Y. Zhang, Anal. Chem. **91**, 548–568 (2019)
68. J. Xu, R. Shi, G. Chen, S. Dong, P. Yang, Z. Zhang, N. Niu, S. Gai, F. He, Y. Fu, J. Lin, ACS Nano **14**, 9613–9625 (2020)
69. N.M. Idris, M.K. Gnanasammandhan, J. Zhang, P.C. Ho, R. Mahendran, Y. Zhang, Nat. Med. **18**, 1580–1585 (2012)
70. M. Ding, D. Chen, D. Ma, P. Liu, K. Song, H. Lu, Z. Ji, ChemPhysChem **16**, 3784–3789 (2015)
71. W. Ren, G. Lin, C. Clarke, J. Zhou, D. Jin, Adv. Mater. **32**, 1901430 (2020)
72. X. Yu, H. Zhang, J. Yu, Aggregate **2**, 20–34 (2021)
73. H. Liu, L. Yan, J. Huang, Z. An, W. Sheng, B. Zhou, J. Phys. Chem. Lett. **13**, 2306–2312 (2022)
74. L. Yan, J. Huang, Z. An, Q. Zhang, B. Zhou, Nano Lett. **22**, 7042–7048 (2022)
75. Y. Xie, Y. Song, G. Sun, P. Hu, A. Bednarkiewicz, L. Sun, Light: Sci. Appl. **11**, 150 (2022)
76. X. Chen, T. Sun and F. Wang, Chem –Asian J., 2020, **15**, 21–33
77. A. Fernandez-Bravo, K. Yao, E.S. Barnard, N.J. Borys, E.S. Levy, B. Tian, C.A. Tajon, L. Moretti, M.V. Altoe, S. Aloni, K. Beketayev, F. Scotognella, B.E. Cohen, E.M. Chan, P.J. Schuck, Nat. Nanotechnol. **13**, 572–577 (2018)

78. H. Zhu, X. Chen, L.M. Jin, Q.J. Wang, F. Wang, S.F. Yu, ACS Nano **7**, 11420–11426 (2013)
79. Q. Liu, Y. Zhang, C.S. Peng, T. Yang, L.-M. Joubert, S. Chu, Nat. Photonics **12**, 548–553 (2018)
80. Y.I. Park, K.T. Lee, Y.D. Suh, T. Hyeon, Chem. Soc. Rev. **44**, 1302–1317 (2015)
81. J. Zhou, C. Li, D. Li, X. Liu, Z. Mu, W. Gao, J. Qiu, R. Deng, Nat. Commun. **11**, 4297 (2020)
82. X. Guo, Y. Yuan, J. Liu, S. Fu, J. Zhang, Q. Mei, Y. Zhang, Anal. Chem. **93**, 3010–3017 (2021)
83. W. Wu, D. Mao, S. Xu, Kenry, F. Hu, X. Li, D. Kong, B. Liu, Chem, 2018, **4**, 1937–1951
84. A.V. Kachynski, A. Pliss, A.N. Kuzmin, T.Y. Ohulchanskyy, A. Baev, J. Qu, P.N. Prasad, Nat. Photonics **8**, 455–461 (2014)
85. X. Xiao, B. Zheng, Q. Zheng, Z. Lu, D. Cen, X. Cai, X. Li, R. Deng, J. Mater. Chem. B **10**, 4501–4508 (2022)
86. L. Zhou, Y. Fan, R. Wang, X. Li, L. Fan and F. Zhang, Angew. Chem., Int. Ed., 2018, **57**, 12824–12829
87. J. Liu, J. Zhang, Chem. Rev. **120**, 2123–2170 (2020)
88. Z. An, J. Huang, L. Yan, L. He, B. Zhou, J. Phys. Chem. Lett. **13**, 9007–9013 (2022)
89. H. Bao, W. Wang, X. Li, X. Liu, L. Zhang, X. Yan, Y. Wang, C. Wang, X. Jia, P. Sun, X. Kong, H. Zhang, G. Lu, Adv. Opt. Mater. **10**, 2101702 (2022)
90. D. Hudry, A. De Backer, R. Popescu, D. Busko, I.A. Howard, S. Bals, Y. Zhang, A. Pedrazo-Tardajos, S. Van Aert, D. Gerthsen, T. Altantzis, B.S. Richards, Small **17**, 2104441 (2021)
91. L. Liu, X. Li, Y. Fan, C. Wang, A.M. El-Toni, M.S. Alhoshan, D. Zhao, F. Zhang, Chem. Mater. **31**, 5608–5615 (2019)
92. S. Fischer, N.D. Bronstein, J.K. Swabeck, E.M. Chan, A.P. Alivisatos, Nano Lett. **16**, 7241–7247 (2016)
93. C. Lee, E.Z. Xu, Y. Liu, A. Teitelboim, K. Yao, A. Fernandez-Bravo, A.M. Kotulska, S.H. Nam, Y.D. Suh, A. Bednarkiewicz, B.E. Cohen, E.M. Chan, P.J. Schuck, Nature **589**, 230–235 (2021)
94. D. Hudry, I.A. Howard, R. Popescu, D. Gerthsen, B.S. Richards, Adv. Mater. **31**, 1900623 (2019)